



# Testbeam studies of pre-prototype silicon strip sensors for the LHCb UT upgrade project

A. Abba<sup>1</sup>, M. Artuso<sup>2</sup>, S. Blusk<sup>2,6</sup>, T. Britton<sup>2</sup>, A. Davis<sup>3</sup>, A. Dendek<sup>4</sup>, B. Dey<sup>5</sup>, S. Ely<sup>2</sup>,  
J. Fu<sup>1</sup>, P. Gandini<sup>2</sup>, F. Lionetto<sup>5</sup>, P. Manning<sup>2</sup>, B. Meadows<sup>3</sup>, R. Mountain<sup>2</sup>, N. Neri<sup>1</sup>,  
M. Petruzzo<sup>1</sup>, M. Pikies<sup>4</sup>, T. Skwarnicki<sup>2</sup>, T. Szumlak<sup>4</sup>, J. C. Wang<sup>2</sup>

<sup>1</sup>*Instituto Nazionale di Fisica Nucleare - Sezione di Milano, Italy*

<sup>2</sup>*Syracuse University, Syracuse, NY USA*

<sup>3</sup>*University of Cincinnati, Cincinnati, OH USA*

<sup>4</sup>*AGH - University of Science and Technology, Faculty of Physics and Applied Computer Science, Kraków,  
Poland*

<sup>5</sup>*Physik-Institut, Universität Zürich, Zürich, Switzerland*

<sup>6</sup>*European Organization for Nuclear Research (CERN), Geneva, Switzerland*

## Abstract

The LHCb experiment is preparing for a major upgrade in 2018-2019. One of the key components in the upgrade is a new silicon tracker situated upstream of the analysis magnet of the experiment. The Upstream Tracker (UT) will consist of four planes of silicon strip detectors, with each plane covering an area of about 2 m<sup>2</sup>. An important consideration of these detectors is their performance after they have been exposed to a large radiation dose. In this article we present test beam results of pre-prototype n-in-p and p-in-n sensors that have been irradiated with doses up to  $4.0 \times 10^{14} n_{\text{eq}}/\text{cm}^2$ .

Submitted to Nucl. Instrum. Meth. A.

© CERN on behalf of the LHCb collaboration, licence CC-BY-4.0.



# 1 Introduction

The Upstream Tracker (UT) detector is a key part of the LHCb Upgrade, replacing the current Tracker Turicensis (TT) stations [1, 2]. The UT, like the TT, is situated just in front of LHCb’s dipole analysis magnet. In this position, it provides a crucial link between segments reconstructed in the upgraded vertex detector [3] and the tracking chambers downstream [4] of the LHCb magnet. It provides a factor of 3 improvement in speed for the tracking in the the fully-software-based trigger [5], reduces the rate of fake tracks being formed by a factor of 2-3, and improves the momentum resolution by about 25% relative to tracks not using UT hits. As a result, the physics scope of the upgrade is greatly enhanced with the UT detector.

The UT detector consists of four silicon planes, each about 1.53 m in width and 1.34 m in height. Each plane is composed of 1.5 m long *staves* that are tiled with  $\sim 10\text{ cm} \times 10\text{ cm}$  silicon wafers. Consecutive wafers are mounted on opposite sides of the stave to ensure no gaps along the height, and adjacent staves are also overlapped to ensure no gaps in the horizontal direction. The majority of the detector area utilizes sensors with an approximate pitch of  $190\ \mu\text{m}$ , however the inner region features sensors with half the pitch ( $95\ \mu\text{m}$ ) to cope with higher occupancy. Both n-in-p and p-in-n type sensors are being considered for

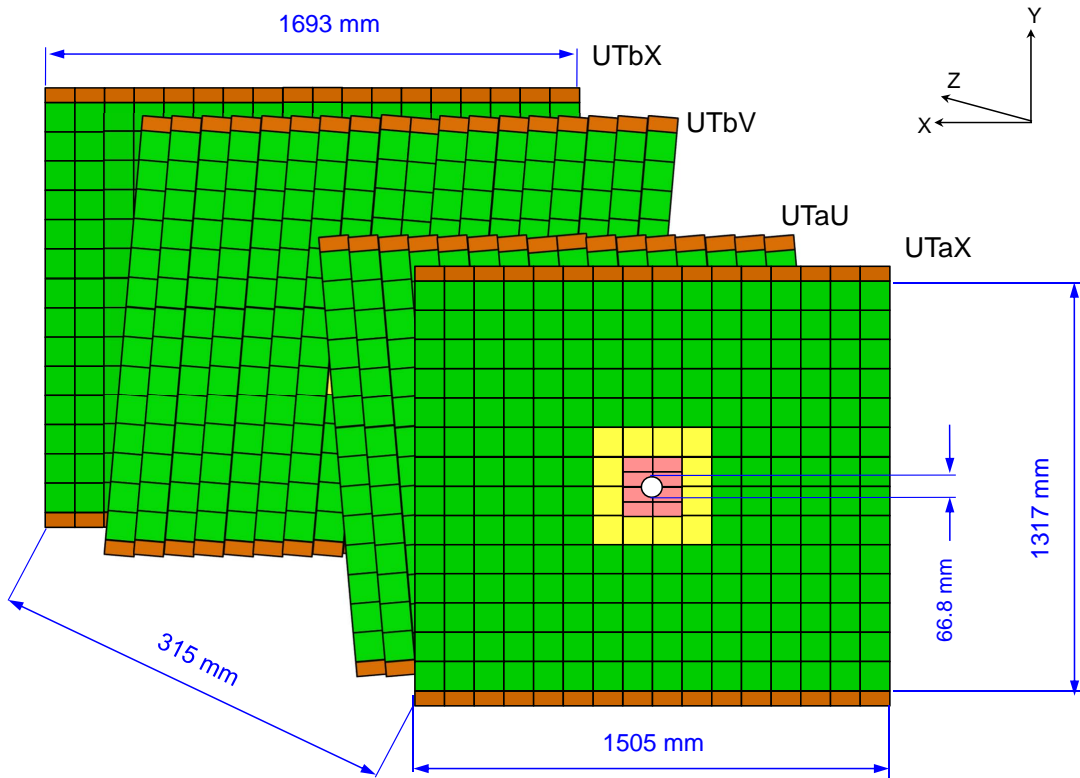


Figure 1: Cartoon showing the layout and dimensions of the four UT planes.

the outer region, but for the inner region, only n-in-p are being considered due to better radiation hardness. For the innermost region of the UT, the largest dose expected, with a safety factor of about two, is about  $5 \times 10^{14} n_{\text{eq}}/\text{cm}^2$ . Outside this region, the dose is not expected to exceed about  $2 \times 10^{13} n_{\text{eq}}/\text{cm}^2$ .

The goals of this test beam were to quantify the performance of several sensor pre-prototypes from Micron Semiconductor, Ltd [6] after a high radiation dose, and compare to corresponding results from similar unirradiated detectors. The properties investigated include, but are not limited to:

- Landau distributions as a function of bias voltage;
- Cluster size versus bias voltage and angle of incidence;
- Charge collected versus interstrip position;
- Resolution versus angle;
- Characteristics of sensors near the quarter-circle region (these emulate the sensors surrounding the beam pipe).

## 2 Experimental setup

The test beam discussed in this article was conducted in October 2014 at the SPS at CERN. The beam consisted of protons with momentum of 180 GeV/c. The beam was delivered in spills at rate of about 4 spills/minute, with each spill lasting about 4 seconds. For most of the data taking, the beam size was collimated down to about 0.5 cm in diameter and each spill provided a particle rate of order 1 MHz.

### 2.1 Telescope description

The pre-prototype UT sensors, or detectors under test (DUT), were studied using the TimePix3 (TP3)-based telescope [7], composed of 8 pixel planes. Each pixel plane is about 1.4 cm  $\times$  1.4 cm and has a pixel size of 55  $\mu\text{m}$   $\times$  55  $\mu\text{m}$ . The planes are tilted in order to provide more charge sharing, and thus better position resolution. A cartoon of the telescope layout is shown in Fig. 2. With the high momentum beam of 180 GeV/c, the reconstructed tracks provide excellent pointing resolution of order 3-4  $\mu\text{m}$  at the DUT. The telescope readout does not require an external trigger: hits are recorded continuously once a run is started. For each pixel hit, both position and a time-stamp with sub-ns precision is recorded. Tracks are then formed (offline) by combining hits that have compatible time values.

### 2.2 Detectors under test

The *mini-sensor* pre-prototypes tested in the October 2014 test beam were obtained from Micron Semiconductor, Ltd [6]. One of the sensors tested was a p-in-n, and six were

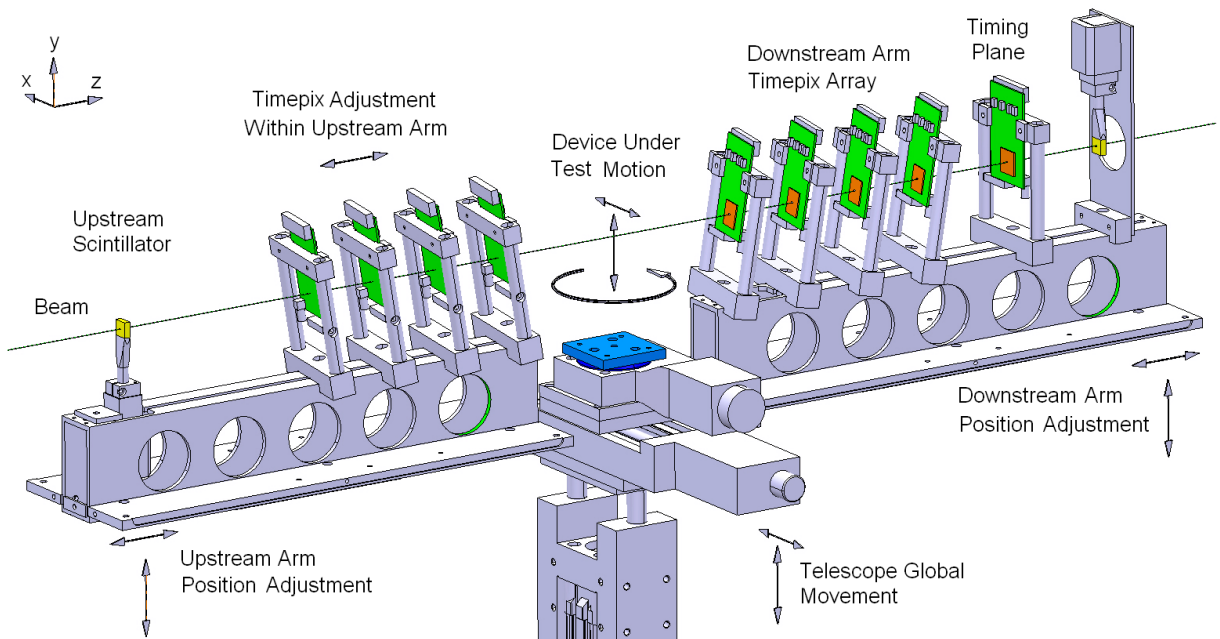


Figure 2: Cartoon showing the TimePix3 telescope used to study the UT sensors.

n-in-p. The resistivities of the sensors, as determined from capacitance versus voltage measurements, were about  $8.8 \Omega \text{ cm}$  for the p-in-n sensor and about  $28 \Omega \text{ cm}$  for the n-in-p. Each sensor was  $1.115 \text{ cm} \times 1.125 \text{ cm}$  in size with a nominal thickness of  $250 \mu\text{m}$ , and had 128 strips with a strip pitch of  $80 \mu\text{m}$  and a strip (implant) width of  $30 \mu\text{m}$ . A schematic of the mini-sensors is shown in Fig. 3. In this schematic, the strips run horizontally. Of the six n-in-p sensors tested, three had the strips terminate such that they form a quarter-circle inactive region of the sensor. Two different guard-ring structures were implemented, as shown in Fig. 3. More details of the sensors under test are shown in Table 1. The MBP1 and MBP2 sensors are differentiated by the guard ring structures, and are shown on the left and right side of Fig. 3, respectively.

Six of the seven sensors were irradiated at the Massachusetts General Hospital (MGH) proton irradiation facility in June 2014, with fluences ranging from  $0.27 \times 10^{14} n_{\text{eq}}/\text{cm}^2$  to  $4.0 \times 10^{14} n_{\text{eq}}/\text{cm}^2$ . Between the time of the irradiation in June 2014, and the test beam in October 2014, the sensors were kept in a freezer, at a temperature below  $-10 \text{ }^\circ\text{C}$ . The sensors were warmed up to room temperature for no more than 7 days to transport the sensors and for wirebonding.

The DUT readout for this testbeam was based on the Alibava DAQ system [8–11], which uses Beetle chips [12,13] as the front end ASIC. The main components of the Alibava system are a customizable detector board to which sensors are mounted, a *daughterboard* that includes two Beetle chips (128 channels each), and a *motherboard* that manages the data flow to/from the Beetle chips and to/from the data acquisition PC.

The DUT was housed in an Aluminum box to provide both shielding and a light-tight environment. A Peltier device was used to cool the sensor to about  $-13 \text{ }^\circ\text{C}$ , and a continuous

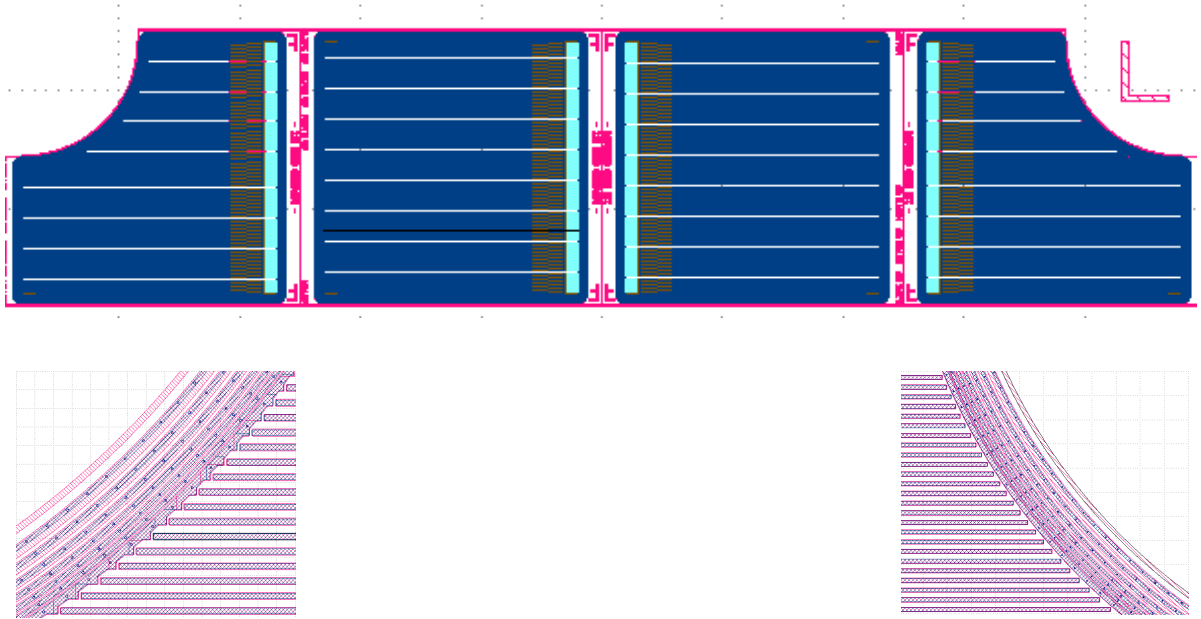


Figure 3: Schematic of the mini-sensors tested during the October 2014 test beam. The two sensors in the middle are full mini-sensors, while the ones on the left and right have a quarter-circle cut out. The difference between the left-most and right-most sensors is in the guard-ring structure, as shown below.

Table 1: Specific details of the sensors tested in the October 2014 test beam. Here,  $\rho$  refers to the resistivity of the silicon and  $N_{e,h}$  indicates either the electron or hole concentration. For sensor 3091-10-MBP2, CV measurements were not available.

Sensor ID	Type	Dose ( $10^{14} n_{eq}/cm^2$ )	$\rho$ ( $\Omega$ cm)	$N_{e,h}$ ( $10^{14} cm^{-3}$ )	Other spec.
3092-1-MS2	p-in-n	0.27	5.1	8.7	250 $\mu$ m
3091-8-MS1	n-in-p	1.0	5.0	27.9	242 $\mu$ m, p-spray
3091-10-MBP2	n-in-p	0.0	n/a	n/a	238 $\mu$ m, p-spray
3091-7-MS2	n-in-p	4.0	5.0	27.6	254 $\mu$ m, p-spray
3091-7-MS1	n-in-p	1.8	4.9	28.5	254 $\mu$ m, p-spray
3091-8-MBP2	n-in-p	4.0	5.2	26.9	242 $\mu$ m, p-spray
3091-8-MBP1	n-in-p	4.0	5.0	27.9	242 $\mu$ m, p-spray

nitrogen flow maintained the relative humidity close to zero. The entire box was mounted on a stage that allowed for horizontal and vertical translations, as well as rotations about the vertical axis to allow for studies of the detector performance versus particle incident angle. The system was equipped with both temperature and relative humidity monitoring.

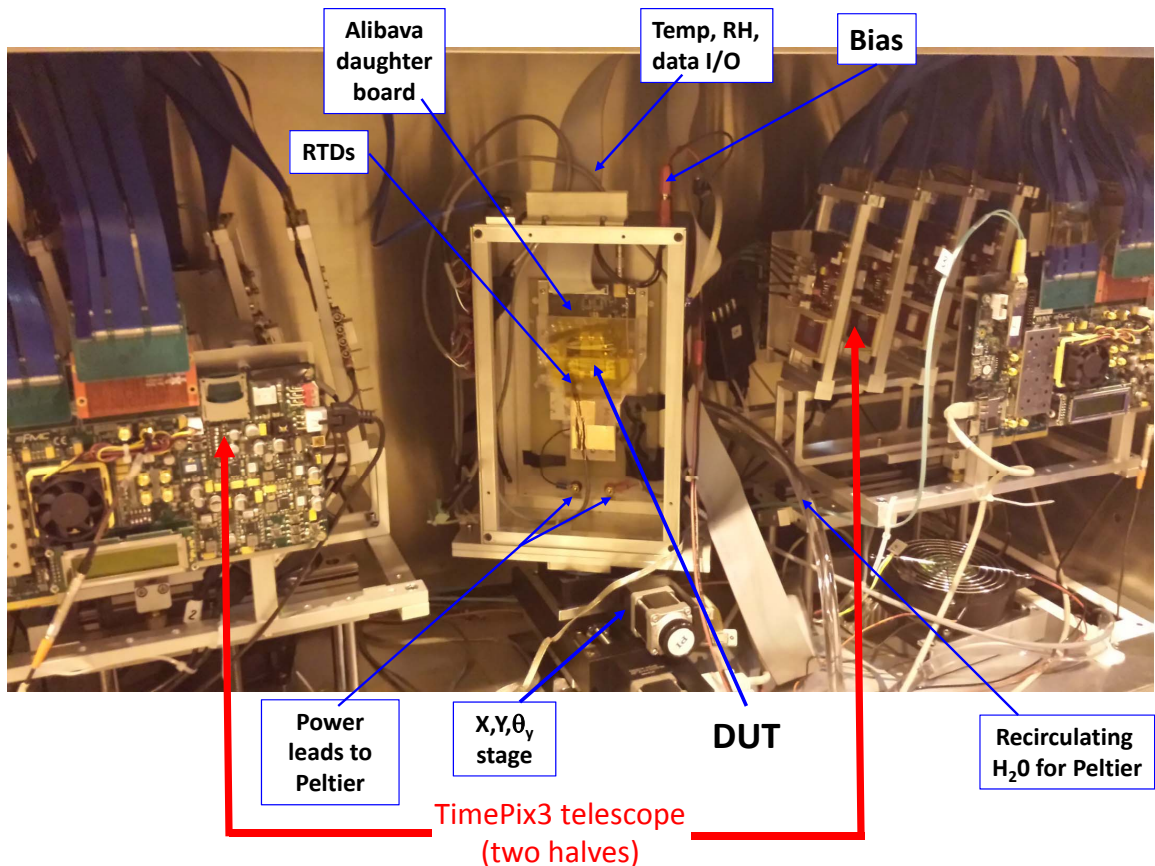


Figure 4: Photograph of the TimePix3 telescope and the DUT during installation at the SPS, together with a description of the different components.

A photograph of the telescope with the UT DUT being installed is shown in Fig. 4. Various components are indicated.

### 2.3 Trigger and synchronization

The trigger was formed from the coincidence of two scintillators (see Fig. 2) and a **not-busy** signal from the Alibava motherboard. This trigger signal was fanned out to both the TimePix3 telescope and the Alibava motherboard. Because the data acquisition systems of the TimePix3 telescope and the DUT were independent of one another, the common trigger signal was used to synchronize the two systems. The signal sent to the Alibava system initiated a readout of the DUT, while the signal sent to the TimePix3 system produced a timestamp in the TimePix3 event record. This timestamp used the same clocks used to time stamp the pixel hits, and in this way, pixel hits could be associated

with a specific trigger. Since the number of time stamps in the TimePix3 event record was identical to the number of triggers sent to the Alibava system, the synchronization only required matching the first event in the Alibava system with the pixel hits/tracks associated to the first trigger time stamp, and then the second event matched to the second trigger time stamp, and so on. In this way, the beam tracks reconstructed in the TimePix3 system were properly matched to the corresponding hits produced in the DUT.

### 3 Corrections and calibrations

Before being able to quantify the performance of the sensors, various calibrations and corrections were applied. These corrections included pedestal and common-mode noise suppression, a cross-talk correction, an out-of-time correction, and are detailed below.

#### 3.1 Calibration scans

Calibration scans, which were taken periodically during the test beam, showed that 1 ADC was equivalent to about  $275 e^-$ . The exact value varied by a few percent, depending on the sensor/readout board. Since the calibration circuit has its own inherent parasitic capacitances, we estimate that there is an inherent uncertainty in the overall calibration not larger than about 5%. Charges presented throughout this article are given in terms of ADC counts, and must be multiplied by 275 to obtain the corresponding charge in number of electrons.

#### 3.2 Pedestal and common mode noise suppression

Pedestals are calculated from datasets of  $10^4 - 10^5$  events recorded during beam stops and are then subtracted from the beam-on runs recorded under the same conditions. Dead or noisy strips are excluded from all parts of the analysis. The pedestal of a given Beetle channel is evaluated as the mean of the raw ADC counts of that channel over the whole pedestal run, after excluding anomalously large or small ADC values. After subtracting the pedestals, the common mode noise is computed (event-by-event) as the average ADC value in a given chip, and is then subtracted from each channel. After the pedestal and common mode noise suppression, the noise level is about 3.5 ADC counts, or about 1000 electrons.

#### 3.3 Cross-talk correction

From analysis of the data, it was found that there was cross-talk between the  $N^{\text{th}}$  and the  $(N+1)^{\text{th}}$  channel. The effect was easily seen by studying the charge asymmetry between the  $(N-1)^{\text{th}}$  and  $(N+1)^{\text{th}}$  channel about the peak strip ( $N$ ) in a cluster with tracks at normal incidence. Due to capacitive coupling some charge sharing is expected, but it should not be asymmetric. The asymmetry is studied for even and odd-numbered peak strips separately. The resulting asymmetries are shown in Fig. 5 (top) before the correction

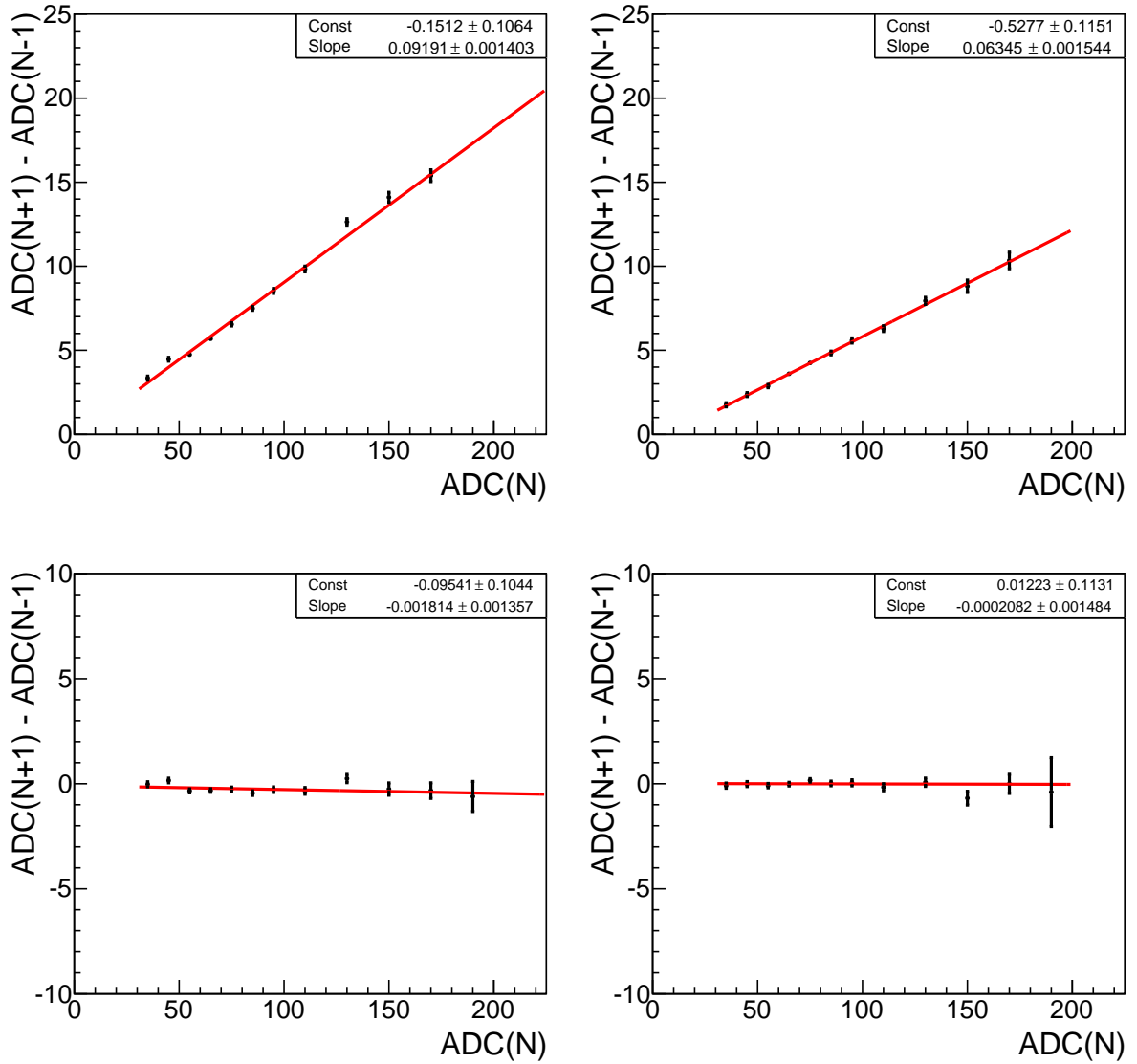


Figure 5: Mean of the difference in charge detected,  $\langle \text{ADC}(N+1) - \text{ADC}(N-1) \rangle$  between the  $(N+1)^{\text{th}}$  and  $(N-1)^{\text{th}}$  strips, as a function of the charge seen in the  $N^{\text{th}}$  strip, for sensor 3092-1-MS2. The top pair of plots show the values for even and odd channels before the correction, the bottom pair after the correction. Plots with an even peak strip numbers are shown on the left, while plots with an odd peak strip number are shown on the right.

and (bottom) after the linear correction for one of the DUTs. The even channels show a larger cross-talk than the odd channels. An empirical correction based on the linear fit shown is applied, and the asymmetry after the correction is shown. This is believed to be due to a sub-optimal timing of the ADC sampling phase, which was a fixed setting in the firmware of the motherboard. The Beetle chip itself is known to have a small amount of cross-talk [13], but the level is below 2%; thus most of the effect is attributable to the readout. All DUTs have similar odd-even cross-talk corrections. The even/odd cross-talk correction was similar for all of the DUTs, but not identical. Therefore, each sensor had a unique cross-talk correction to remove this bias.

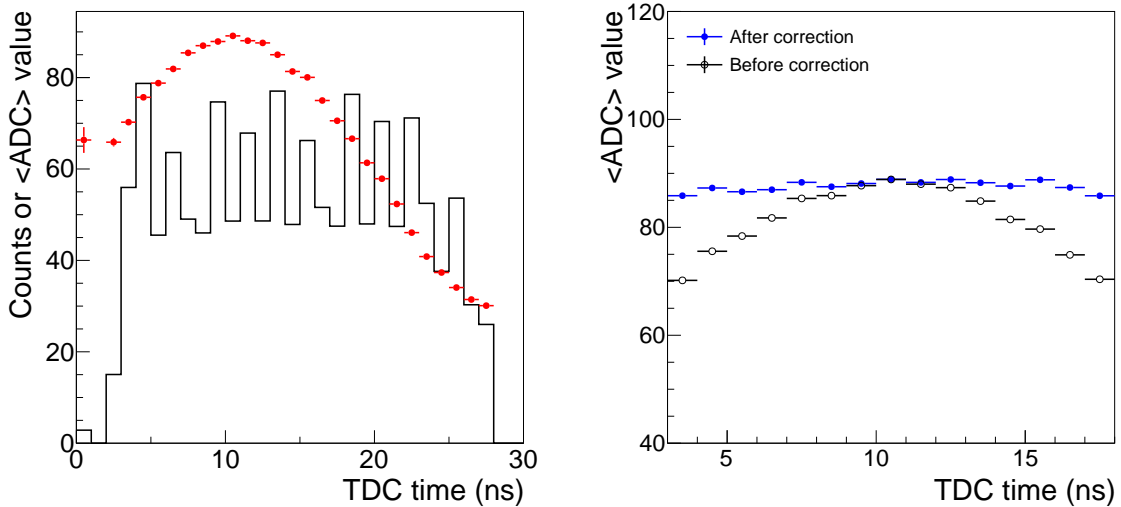


Figure 6: (Left) Raw TDC time spectrum, overlaid with the average ADC versus TDC time for DUT signal clusters. (Right) Average ADC versus TDC time for DUT signal clusters before (black points) and after (blue points) the time correction.

### 3.4 Out-of-time correction

The Alibava system provides a 40 MHz clock to sample the front end of the Beetle chip. However, beam particles arrive asynchronously with respect to this clock. Prior to taking data for analysis, the arrival time of the signal from the DUT was timed in with the signal from the scintillators to ensure that the peak of the Beetle response fell within the 25 ns time window from the previous 40 MHz clock edge. With respect to this clock edge, the Alibava system stores the TDC time for offline selection of signal that arrive in phase with the 40 MHz sampling clock. When timing in the system, we adjusted the latency such that the signal from a beam particle arrives at about 10 ns into this time window. That is, the maximum charge is collected from the Beetle when the TDC time is 10 ns. To make use of the data not precisely at the peak, we include and correct the measured charge for signals within  $\pm 3.5$  ns of the peak. The correction is obtained by fitting the average ADC value for signal clusters as a function of the TDC time to a Gaussian function. In this limited range, the correction is no more than about 5 – 6%. Figure 6(left) shows the raw time spectrum of all triggered events, overlaid with the average ADC for signal clusters as a function of the TDC time. The right panel shows the average ADC versus time before and after the correction, where only the region used in the fit is shown.

### 3.5 Alignment

The coordinate system is defined such that  $X$  is horizontal,  $Y$  is vertical, and  $Z$  is parallel to the beam axis. Sensors are aligned with respect to tracks using the *residual* distribution, which is defined as the difference between the reconstructed  $X$  position of the hit and the

$X$  position of the track extrapolated to the position of the sensor. The degrees of freedom considered are: (i) offsets in the  $X$  direction, (ii) offsets along the  $Z$  axis, (iii) rotations around the  $Z$  axis, and (iv) rotations around the  $Y$  axis. A typical set of alignment plots are shown in Fig. 7, after the alignment is done. The profile plots are close to flat at zero, but do show deviations in the tails of the distributions. As these are profile plots, and they account for only a very small fraction of the events, this is likely a limitation of the profile plot.

## 4 Results

The results of the test beam are presented below, starting with the results obtained from particles striking the detector at normal incidence, and continuing with the dependence on the incidence angle.

### 4.1 Cluster finding in the DUT

Clusters in the DUT are built up by searching for a *seed strip* that has a collected charge more than 20 ADC counts. Moving away from the seed strip, we add adjacent *side strips* having at least 11 ADC counts (about  $3 \times \sigma_{\text{noise}}$ ). The cluster is terminated when a side strip charge is below 11 ADC threshold. Thus, by definition, a cluster has between 1 and 5 strips included; each strip has charge of at least 11 ADC counts, and there is at least one strip with at least 20 ADC counts. Therefore the minimum charge of any cluster is 20 ADC counts. When there are multiple strips in the cluster, the position is computed using linear charge weighting, namely  $\bar{x} = \sum x_i q_i / \sum q_i$ , where  $x_i$  and  $q_i$  are the positions and charges of the strips in the cluster. Better resolution can be achieved with a non-linear correction, but optimizing the resolution on these pre-prototype sensors is not a central goal of this test beam study.

### 4.2 Tracking information

Tracks were reconstructed using the TimePix3 telescope. About 95% of tracks had 8-pixel hits; the remainder was 7-hit tracks. Only tracks with good fit quality were used, by requiring that the  $\chi^2/\text{ndf} < 4$ , where ndf is the number of degrees of freedom. Figure 8 shows the beam profile ( $Y$  vs  $X$ ) for tracks that have a DUT hit within  $100 \mu\text{m}$  from the track. The quarter-circle regions in board 2 chip 1, and board 4 chips 0 and 1 are evident. The sharp vertical edges are due to the collimators in the beamline, and the boundaries along  $Y$  are fiducial cuts used in the analysis. The beam intensity was tuned so that most of the triggered events had a single beam track, although about 10% of events had more than one track. Multi-track events are excluded from the analysis, to ensure that the reconstructed track is the one which produced the trigger.

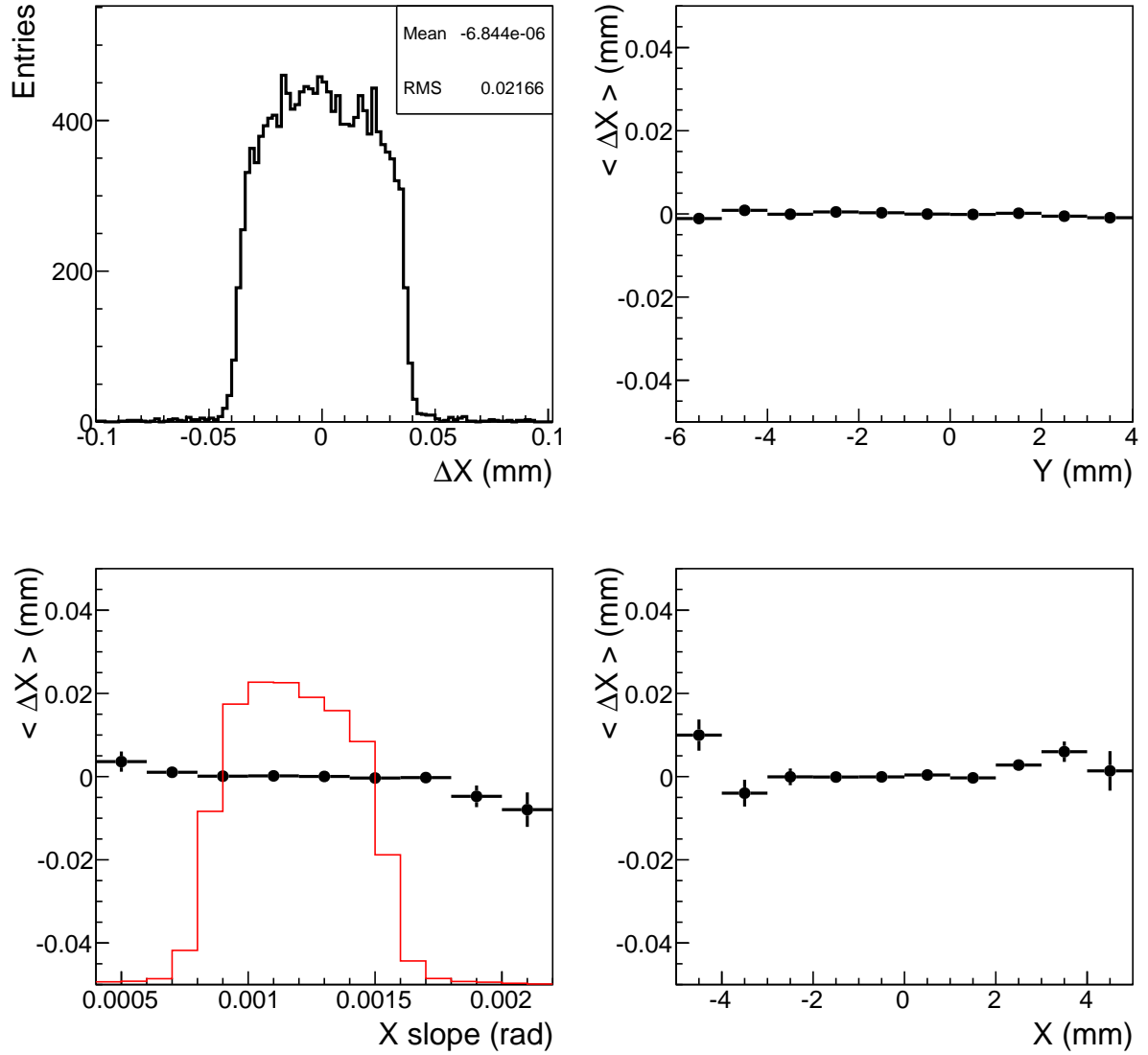


Figure 7: Alignment plots for sensor 3092-1-MS2, after alignment, showing (top left)  $X$  residual, (top right) average  $X$  residual vs  $Y$  position, (bottom left) average  $X$  residual vs  $X$  slope, and (bottom right) average  $X$  residual vs  $X$  position, after the alignment is performed. Superimposed on the bottom left plot is the slope distribution of the tracks.

### 4.3 Single event displays

A few typical events, after all corrections are applied, are shown in Fig. 9. Here, no requirement is made on the number of tracks. Strips with large ADC counts are indicative of the passage of a beam particle through the detector. The other channels show roughly Gaussian fluctuations about zero, typical of incoherent detector noise. Signals generally stand out significantly above the noise.

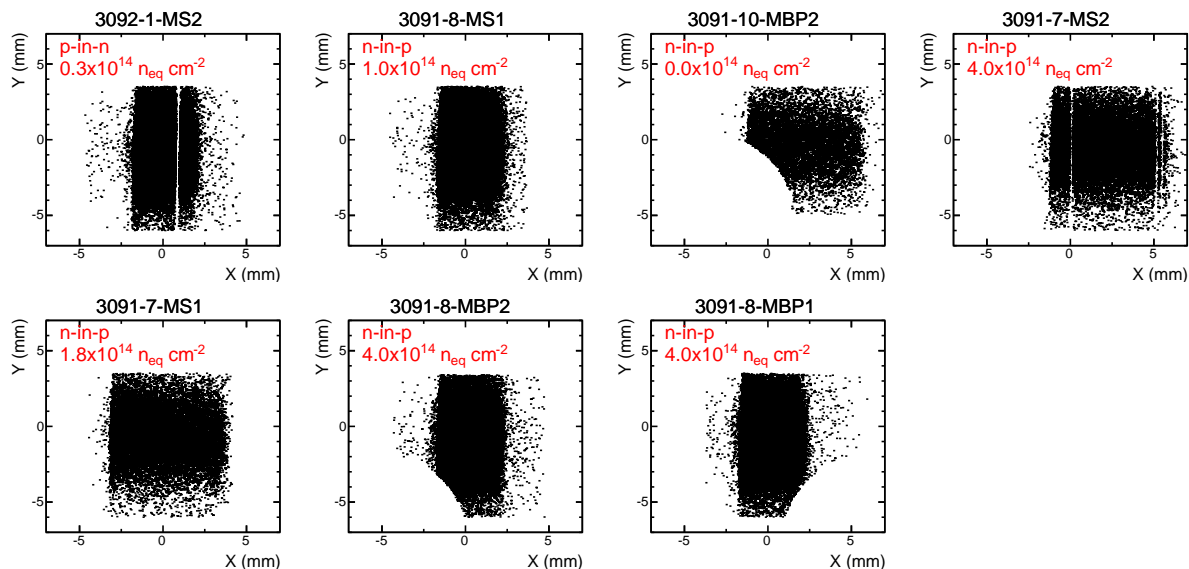


Figure 8: Profile of the beam ( $Y$  vs  $X$ ) at the DUT for each of the 7 sensors for a typical set of runs. The 3 DUTs with the quarter-circle edge are evident in these distributions.

#### 4.4 Noise

To investigate the noise more quantitatively, the distribution of ADC counts on all strips for a typical run of each sensor is shown in Fig. 10. The runs are chosen to be in a range where each detector is fully depleted. While these are beam-on data, the signal contribution to the shown distributions is negligible, since clusters typically have charge  $\sim 70$ -80 ADC counts on average, and are therefore off the plot. In addition, most events have only one cluster among the 255 channels. For each distribution, the core of the distribution is fit to a Gaussian function and show the width, which is found to be in the range of about 3.3–3.5 ADC counts. The gain is roughly  $280 e^-/\text{ADC}$ , so this corresponds to a noise level of about  $1000 e^-$ . Pedestal data with the beam off give compatible results.

#### 4.5 Landau distributions versus bias voltage

The most important aspect of these test beam studies is to validate that the sensors still have a high signal-to-noise ratio (S/N) at the highest expected radiation dose. For each sensor, data was recorded at bias voltages ranging from 50 V (well below full depletion) to 500 V (well above it). A few of the resulting distributions of collected charge for sensor 3091-8-MBP2 (n-in-p,  $4.0 \times 10^{14} n_{\text{eq}}/\text{cm}^2$ ) are shown in Fig. 11. The cluster charge distributions are each fit to a Landau convoluted with a Gaussian function, and the fit parameters are indicated. For bias voltages smaller than 75 V, the fits are biased because of the 20 ADC threshold requirement on the seed strip in the cluster. As the bias voltage increases, so does the collected charge.

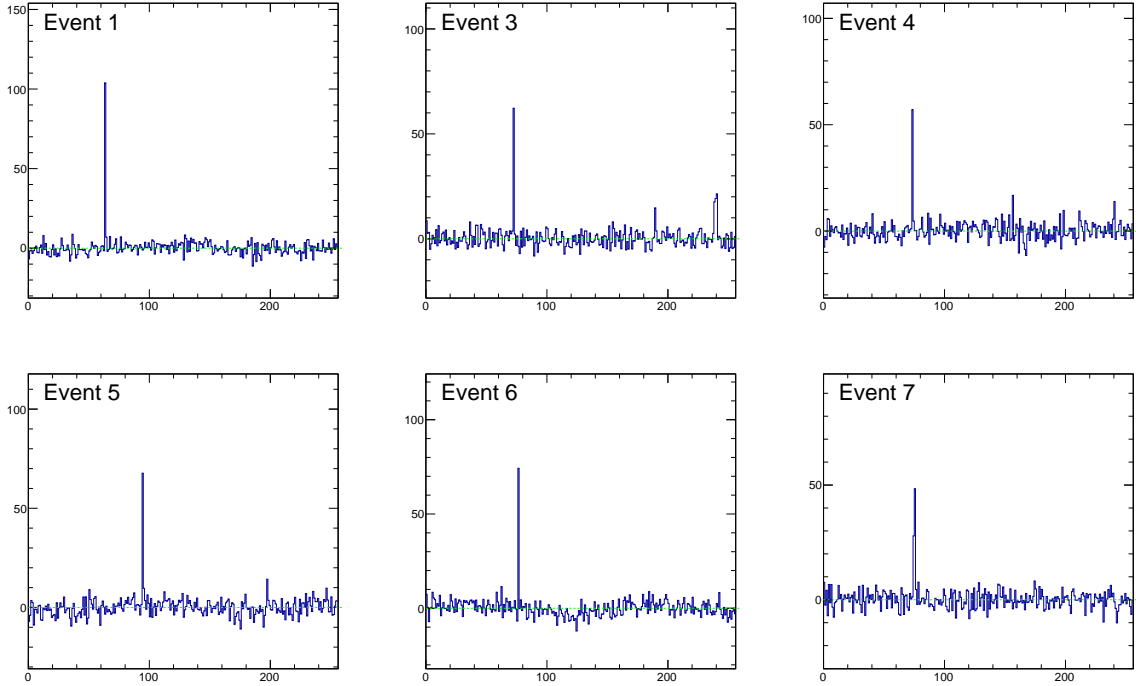


Figure 9: A few examples of single events for sensor 3092-1-MS2 (p-in-n), with a bias voltage of 250 V.

The results for all DUTs tested are summarized in Fig. 12, which shows the most probable value (MPV) of the Landau fit as a function of the bias voltage, for each of the sensors. The p-in-n sensor is shown with a dashed curve and the n-in-p sensors are represented by solid curves. All of the curves exhibit a plateau in the 300 – 400 V range, although there is a clear trend that the sensors with the higher accumulated dose exhibit a lower MPV in the plateau region. Similar loss of collected charge in highly irradiated detectors has been seen previously (see for example Refs. [14–19]). The three highest dose ( $4.0 \times 10^{14} n_{\text{eq}}/\text{cm}^2$ ) sensors show a similar behavior. Since the noise is  $\sim 3.5$  ADC per channel, the S/N is still quite high, about 18 for single strip clusters, even in the most irradiated detectors.

## 4.6 Cluster size

Figure 13 shows the distribution of cluster sizes for the DUTs after all corrections are applied, all at normal incidence, and at bias voltages in the plateau region of Fig. 12. In the p-in-n sensor, about 85% of the clusters are single hit clusters. On the zero dose n-in-p sensor, the single hit cluster fraction is a bit lower, about 82%. The irradiated n-in-p sensors show a substantially larger fraction of 2-strip clusters, of about 40%. The increase in cluster size can be understood as due to incomplete cancellation of the induced charges

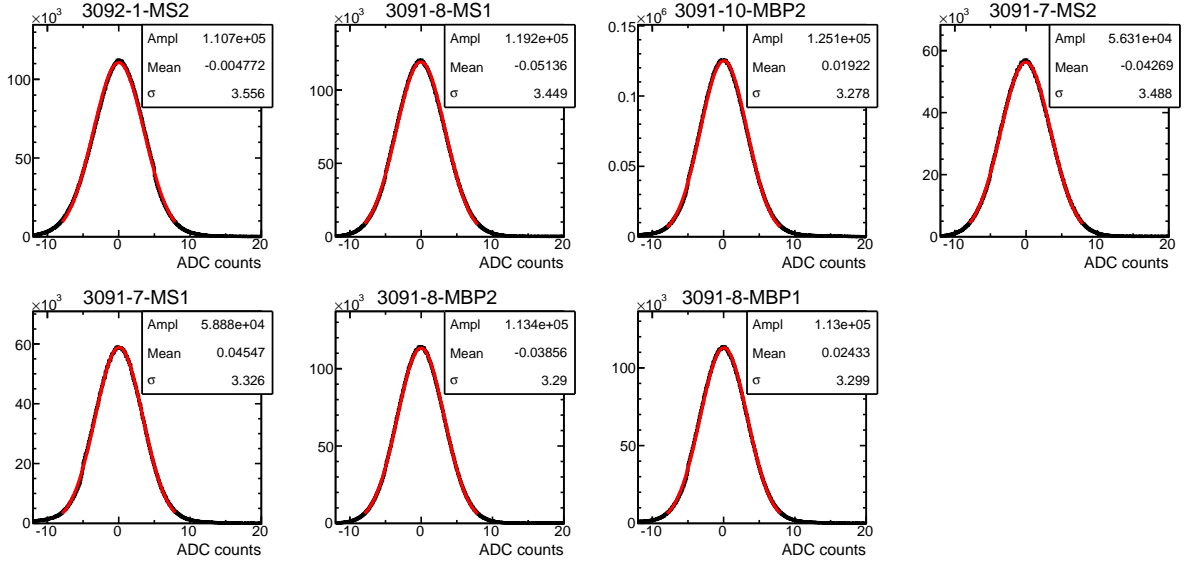


Figure 10: Distributions of ADC counts for the DUTs after all corrections during beam-on runs. The signal is off the right hand side of the plot, and is not visible.

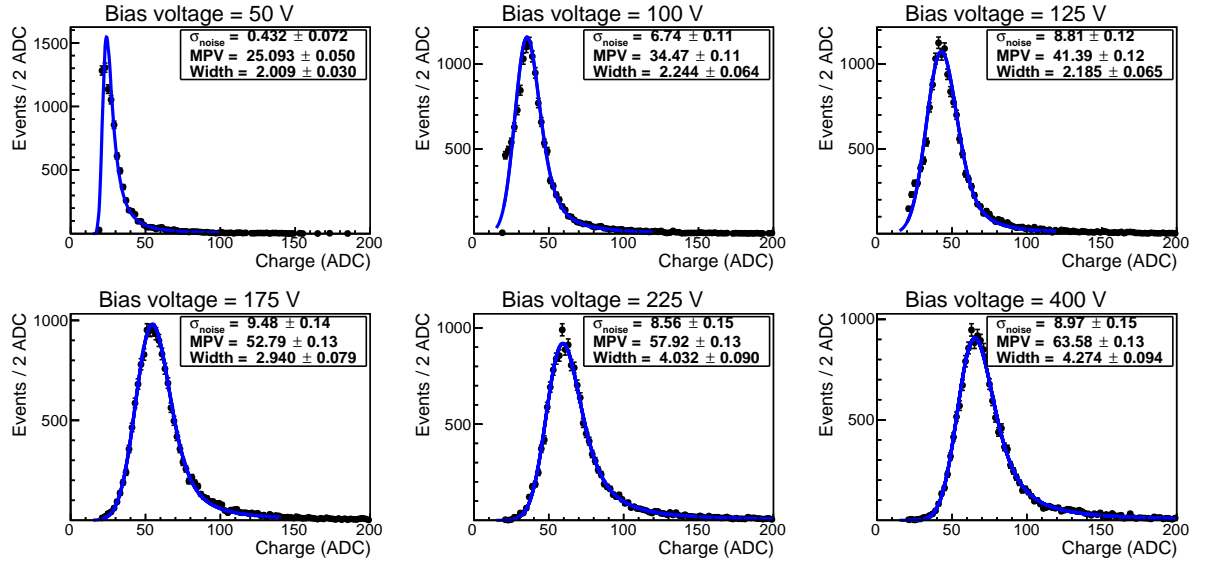


Figure 11: Distributions of ADC counts for sensor 3091-8-MBP2, which is an n-in-p type sensor, irradiated to  $4.0 \times 10^{14} n_{\text{eq}}/\text{cm}^2$ , for several bias voltages. Each distribution is fitted to a Landau convoluted with a Gaussian resolution function and is overlaid.

on neighboring strips due to charge trapping within the bulk and/or underdepletion of the detector [20] This effect, which leads to an increase in the cluster size, dominates over any decrease in cluster size due to the combination of less of the total charge being collected and the fixed ADC thresholds used in the clustering.

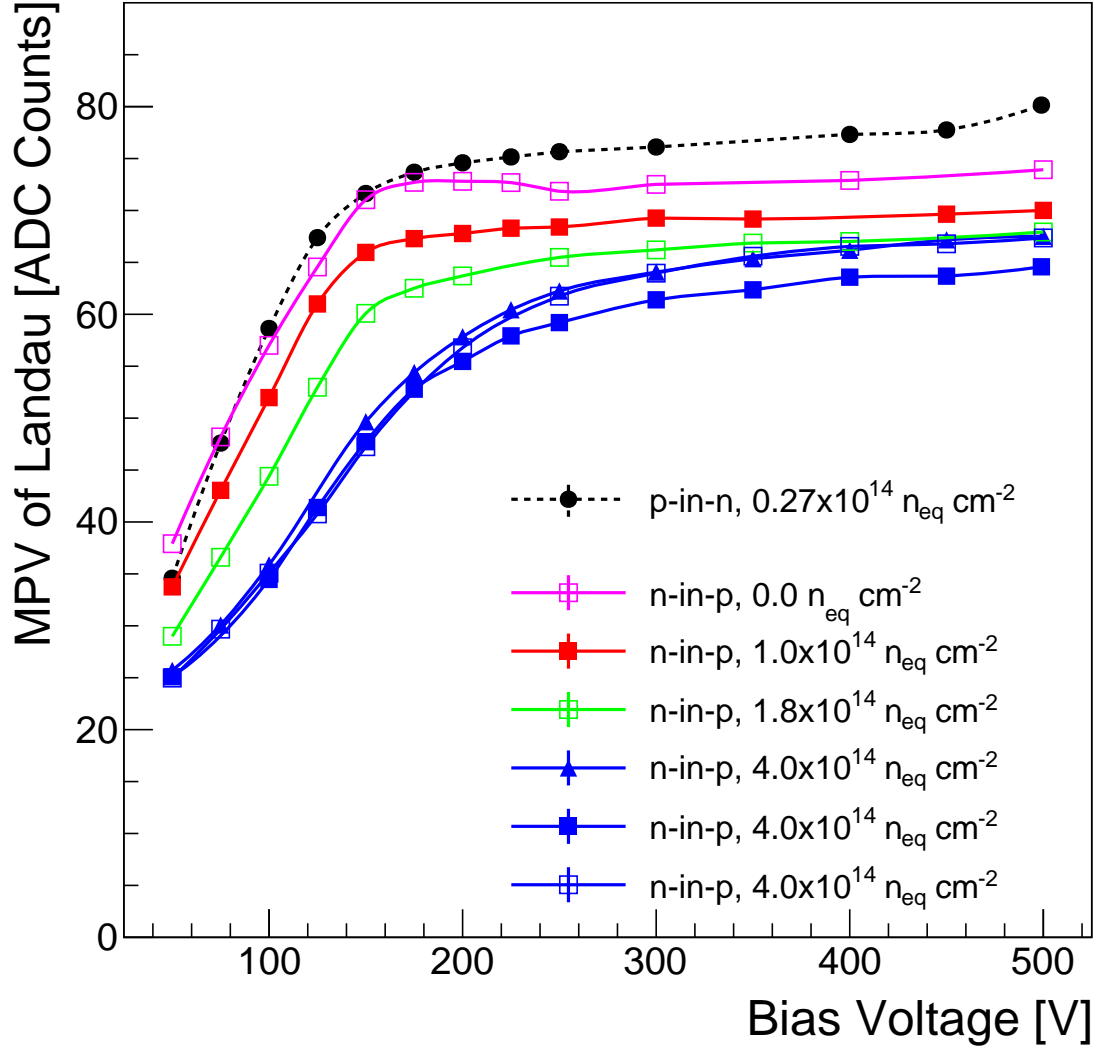


Figure 12: The most probable value of the collected charge from the Landau fit as a function of bias voltage for each of the DUT. Tracks are at normal incidence to the sensor.

#### 4.7 Cluster charge versus cluster size and interstrip position

In this section, we investigate the dependence of the collected charge on the cluster size. With zero thresholds, and no radiation effects, one would expect that the collected charge to be independent of the cluster size. However, radiation effects and non-zero thresholds can lead to a difference. Figure 14 shows the Landau distributions in the plateau region of the sensors, and overlaid are the separate contributions from 1 and 2-strip clusters. The 1-strip and 2-strip clusters have similar MPVs, although not identical. Due to the threshold bias mentioned above, the  $0.27 \times 10^{14} n_{\text{eq}}/\text{cm}^2$  p-in-n and the zero dose n-in-p

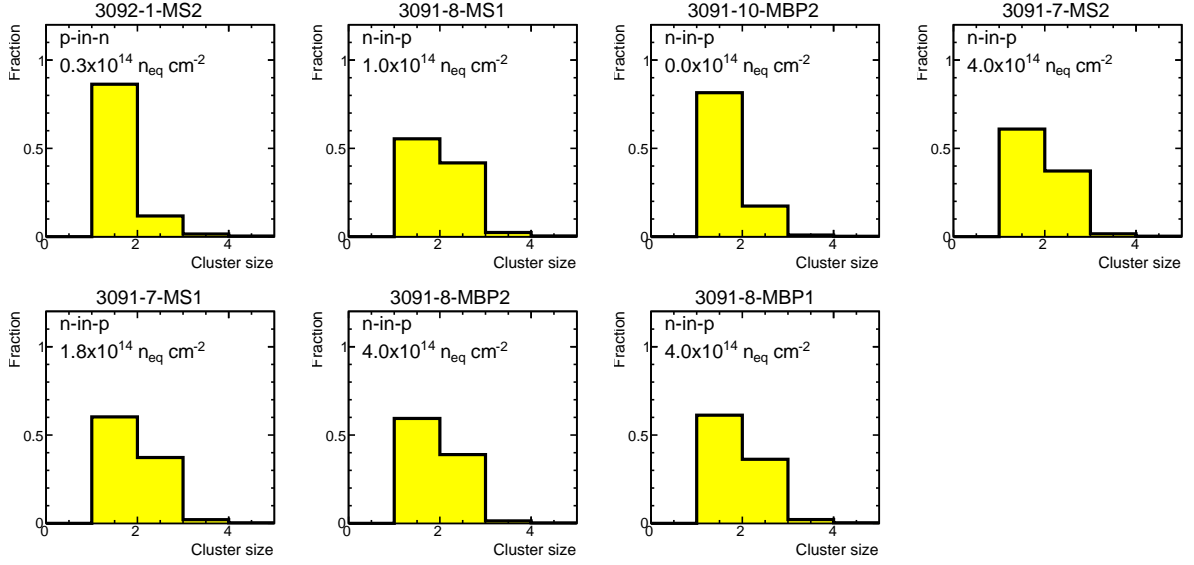


Figure 13: Distributions of the cluster size for the DUTs, after all corrections for tracks at normal incidence. The runs are taken from the plateau region of each DUT.

sensors have larger cluster charge for 2-strip clusters compared to the 1-strip clusters. However, for the irradiated sensors, the opposite is seen, that is, 2-strip clusters have a lower charge collected than 1-strip clusters. From these observations, we conclude that the n-in-p sensors that received the radiation dose (i) have reduced total charge, (ii) have a larger fraction of two-strip clusters, and (iii) have less charge collected in two-strip clusters compared to 1-strip clusters.

Additional information can be gained by investigating the charge collection as a function of the relative position between two strips. For each track, the interstrip position is defined to be the position at the DUT mapped onto the range from  $[0, 1]$ , where 0 is the center of the  $N^{th}$  strip and 1 is the center of the  $(N + 1)^{th}$  strip. The distributions of the average cluster charge as a function of the interstrip position are shown in Fig. 15 for each of the DUTs. It is seen that the heavily irradiated n-in-p sensors exhibit a steady decrease in charge collection as the track approaches the middle region between two strips. At the center, a loss of approximately 15% in collected charge is observed. The p-in-n and unirradiated n-in-p show a small loss in the middle between two strips, but the effect is not more than a few percent. Similar loss of collected charge in the mid-region between two strips in irradiated detectors has been reported in test beams of the ATLAS SCT [17, 21].

From this, it is evident that a sizeable part of the drop in collected charge of the irradiated sensors is due to loss of charge when the track has an interstrip position between 0.2 and 0.8, where a 10-15% loss in charge is seen. When the track has an interstrip position less than 0.2 or greater than 0.8, the loss in collected charge is not as pronounced. Nevertheless, it is the average over the strip which is relevant for the detector performance. The efficiency versus the interstrip position has also been investigated, and in all cases, it is at least 99%. Despite the loss in collected charge, there is no indication of any loss of

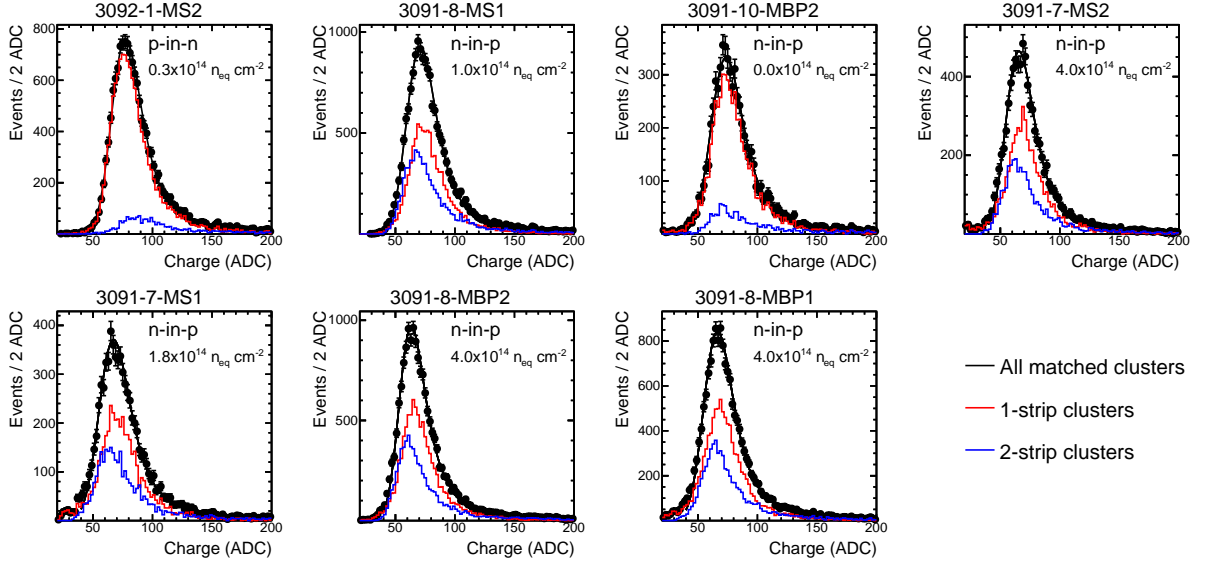


Figure 14: Distributions of charge collected in each DUT in the plateau region for tracks at normal incidence. The black points show all clusters matched within  $100 \mu\text{m}$  of a track, and the colored histograms show 1-strip and 2-strip cluster contributions. The data are fit to a Landau convoluted with a Gaussian resolution function, and the fit is shown.

efficiency.

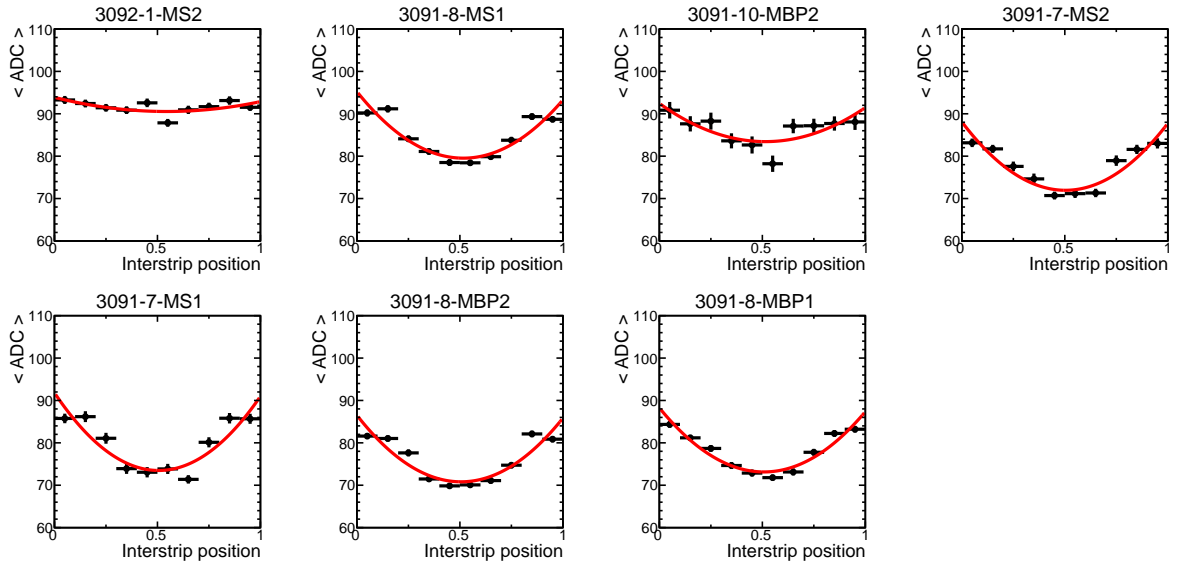


Figure 15: Distributions of the average cluster charge as a function of the relative position within a strip, for tracks at normal incidence. A second order polynomial fit is overlaid just to guide the eye.

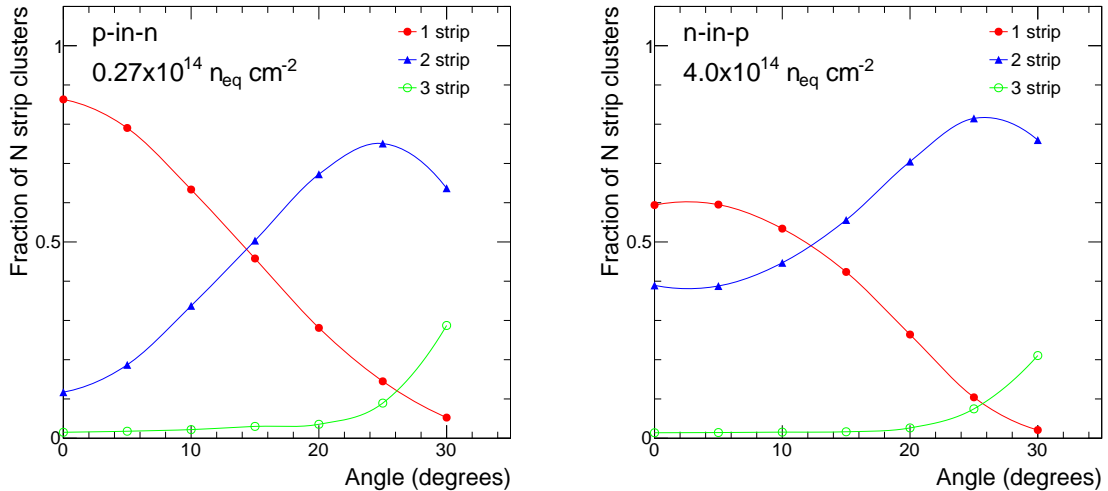


Figure 16: Fraction of 1-strip, 2-strip, and 3-strip clusters as a function of angle for (left) 3092-1-MS2 ( $0.27 \times 10^{14} n_{\text{eq}}/\text{cm}^2$  p-in-n), and (right) 3091-8-MBP2 ( $4.0 \times 10^{14} n_{\text{eq}}/\text{cm}^2$  n-in-p).

#### 4.8 Cluster size and resolution versus angle

Studies of the detector performance were also carried out at angles ranging from normal incidence to  $30^\circ$  (with respect to the normal to the sensor). The fraction of 1, 2 and 3-strip clusters as a function of the angle for (left) the p-in-n sensor and (right) one of the  $4.0 \times 10^{14} n_{\text{eq}}/\text{cm}^2$  n-in-p sensors, is shown in Fig. 16. There is a clear increase in the fraction of 2-strip clusters in both cases, which reaches a maximum at about  $22.5^\circ$ , beyond which the 3-strip clusters start to become sizeable. The main difference between the two sensors is the cluster size at zero angle. For the heavily irradiated detectors, at normal incidence, the 2-strip cluster fraction is significantly larger (see cluster size distributions for normal incidence in Fig. 13).

The residual distributions between the UT hit and the track are shown in Fig. 17 for the  $0.27 \times 10^{14} n_{\text{eq}}/\text{cm}^2$  p-in-n sensor. The angles range from  $0^\circ$  to  $30^\circ$  in  $5^\circ$  steps. The contributions from 1, 2, and 3-strip clusters are also shown. The 3-strip clusters make up only a very small fraction, except at the two largest angles. As the angle increases the resolution improves, as indicated by the RMS of the distributions. The best resolution should be achieved when  $\tan^{-1}(\text{pitch}/\text{thickness}) \sim 18^\circ$ . The RMS is minimum for the  $20^\circ$  angle (RMS =  $10.6 \mu\text{m}$ .) The 2-strip residual distribution is fit to a Gaussian function, and the width returned by the fit,  $\sigma_2$ , is shown. Two-strip clusters provide a resolution of about  $7 \mu\text{m}$  for tracks with angles in the  $15$ - $20^\circ$  range, which is about 3 times better than binary resolution. At small angles, most of the clusters are single strips, and the residual distribution is roughly flat, as one would expect. At very large angles, the 2-strip resolution worsens. This is likely due to a third strip that should have been included in the cluster but was below the minimum ADC side strip threshold to be included. Improved

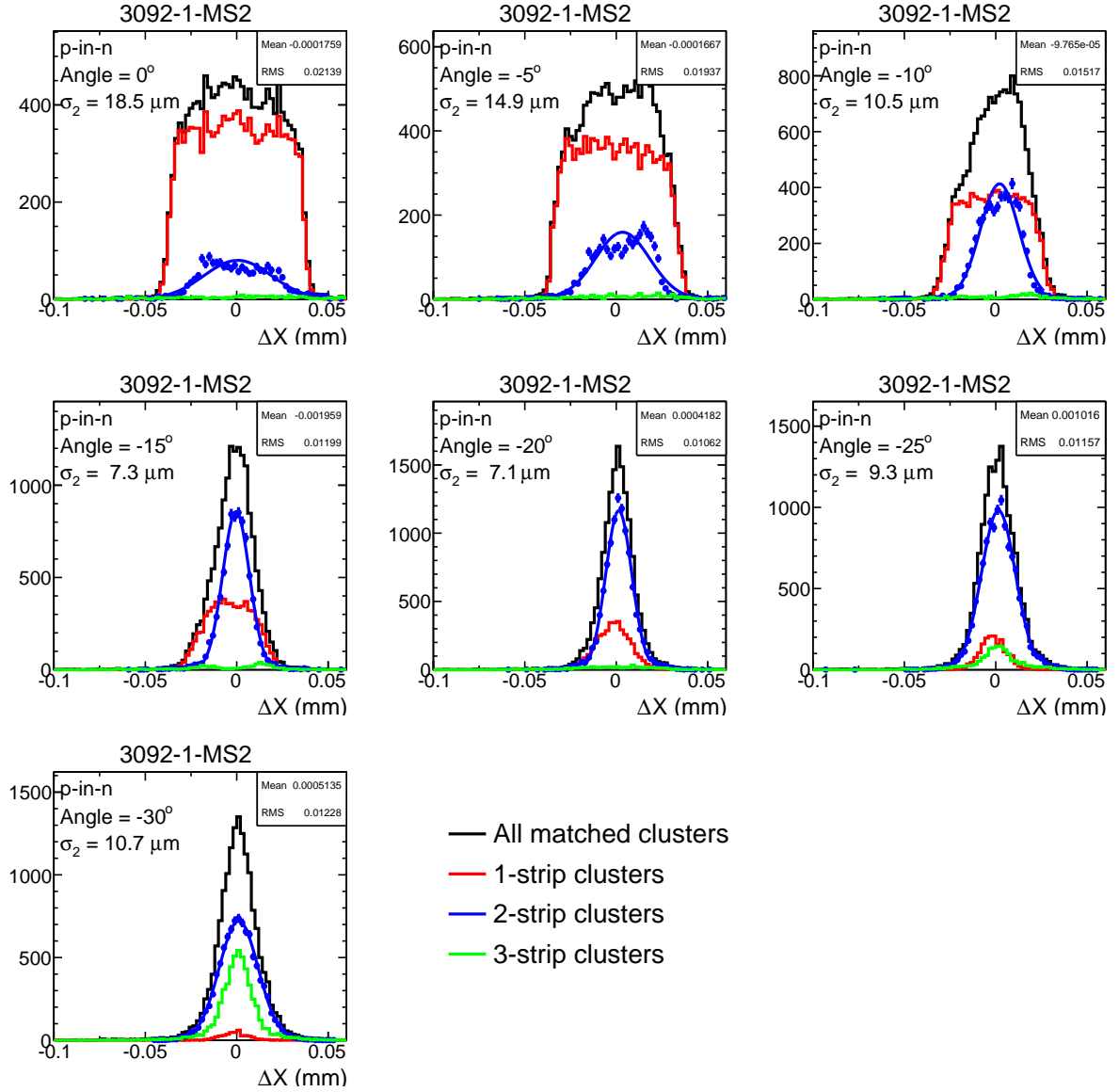


Figure 17: Residual distributions for angles ranging from  $0^\circ$  to  $-30^\circ$  for DUT 3092-1-MS2 ( $0.27 \times 10^{14} n_{\text{eq}}/\text{cm}^2$  p-in-n). The contributions from 1-strip, 2-strip, and 3-strip clusters are also shown. The 2-strip cluster distributions are each fit to a single Gaussian function, and the widths,  $\sigma_2$ , are also indicated.

resolution, primarily for tracks at low incidence angle, was demonstrated by applying a non-linear charge weighting to two-strip clusters, but it is not presented here.

Figure 18 shows the corresponding residual distributions for one of the  $4.0 \times 10^{14} n_{\text{eq}}/\text{cm}^2$  n-in-p sensors. A similar resolution is obtained in the 15-20° angular range, as for the p-in-n sensor. However, the notable difference (with respect to the p-in-n sensor) is that at low angles, the 2-strip contribution is sizeable, and shows the improved resolution that is

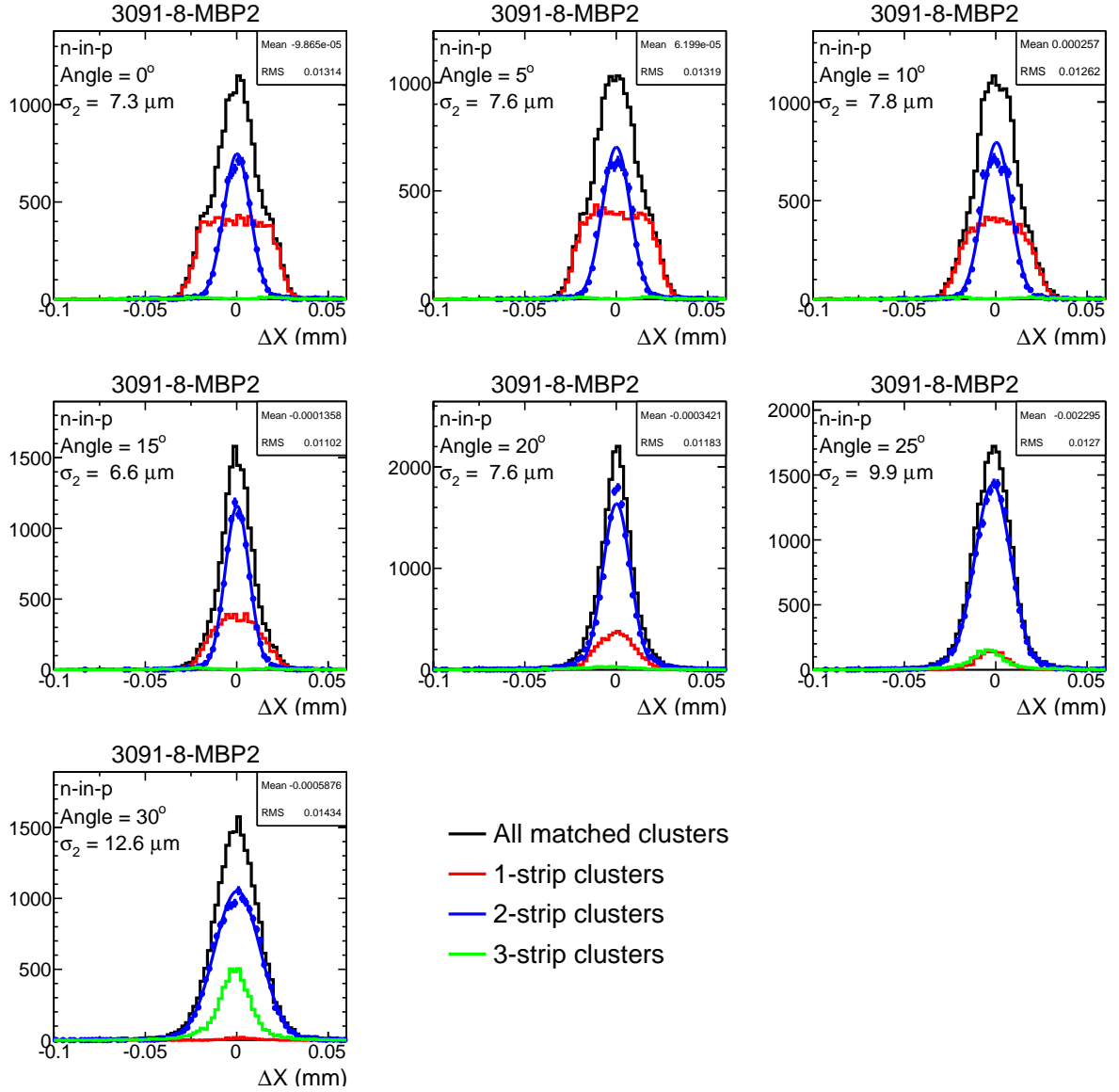


Figure 18: Residual distributions for angles ranging from  $0^\circ$  to  $-30^\circ$  for DUT 3091-8-MBP2 ( $4.0 \times 10^{14} n_{\text{eq}}/\text{cm}^2$  n-in-p). The contributions from 1, 2, and 3-strip clusters are also shown. The 2-strip cluster distributions are each fit to a single Gaussian function, and the widths,  $\sigma_2$ , are also indicated.

generally accompanied by a 2-strip cluster. This clearly illustrates that the larger cluster sizes associated with the irradiated n-in-p sensors are not an anomaly, since they are also accompanied by better position resolution.

The position resolution as a function of the angle is presented for 3 of the sensors in Fig. 19, the  $0.27 \times 10^{14} n_{\text{eq}}/\text{cm}^2$  p-in-n, the  $1.0 \times 10^{14} n_{\text{eq}}/\text{cm}^2$  n-in-p and one of the  $4.0 \times 10^{14} n_{\text{eq}}/\text{cm}^2$  n-in-p sensors. The resolution of the p-in-n sensor increases as one

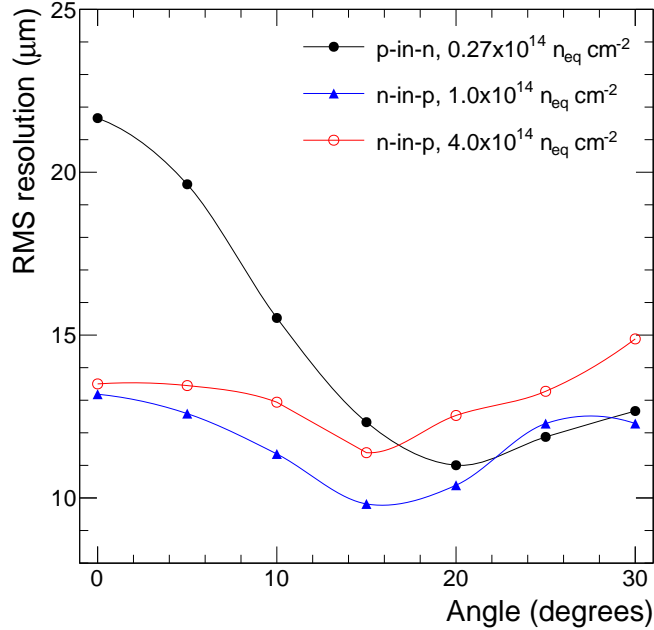


Figure 19: RMS of the residual distribution as a function of angle (with respect to the normal to the sensor) for 3 different sensors.

approaches normal incidence, reaching a maximum of about  $23 \mu\text{m}$ , which is approximately  $80 \mu\text{m}/\sqrt{12}$ . For the n-in-p sensors at normal incidence, the position resolution is much better, about  $13 \mu\text{m}$ , owing to the larger amount of charge sharing between the strips (see Fig. 16). The  $4.0 \times 10^{14} n_{eq}/\text{cm}^2$  irradiated n-in-p sensor shows slightly worse position resolution than the  $1.0 \times 10^{14} n_{eq}/\text{cm}^2$  sensor, but it is only at the  $2 \mu\text{m}$  level in the worst case. This difference is not of great concern for the UT detector.

#### 4.9 Charge collection near the quarter-circle region

Three of the sensors studied during the test beam have a quarter-circle region where there are no strips (see Fig. 3). One of the sensors with this quarter-circle is the unirradiated n-in-p sensor, and the other two are board 4 sensors 0 and 1. The latter two have different guard-ring structures, as shown in Fig. 3. We investigate whether there is any drop in charge collected as one approaches the quarter-circle radially. Using the data, the center of the circle is determined using the 3D information from the TP3 tracks that have matched DUT clusters. The average ADC value as a function of the radial distance from the center of the circle is then analyzed. The results for the 3 sensors are shown in Fig. 20, where each row shows the results for a single sensor. The left column shows the XY profile of tracks that have matched DUT hits, along with an arc that shows the estimated circle to match the quarter-circle region void of strips. The right hand plots show an overlay of

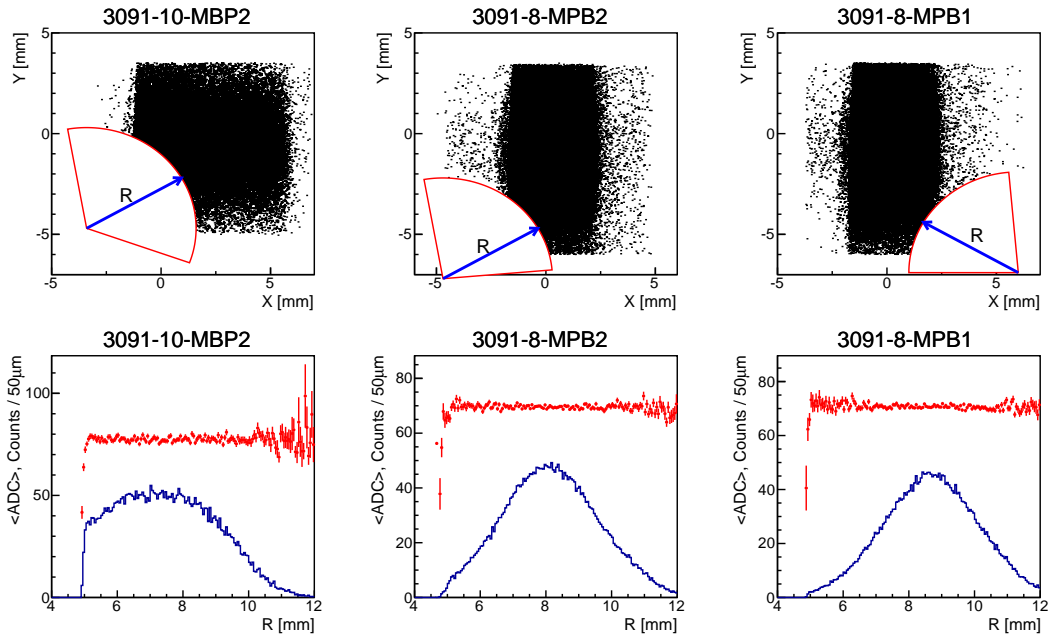


Figure 20: (Left column) XY distributions of tracks matched to clusters for each of the 3 mini beam-pipe sensors. (Right column) Overlay of average ADC value vs radial coordinate (red with error bars) and the radial distribution of tracks at the DUT (blue histogram). The radius is computed using the center of the red circles shown in the left column.

the radial distribution of tracks with matched DUT hits, with the average ADC value of clusters as a function of the radius. In this figure, several runs with bias voltage above 350 V are combined, and the average ADC is the raw value with no TDC time requirement. This is done to increase the sample size, as the main interest is to uncover a trend, while the absolute value is of less concern.

There is no clear indication of large loss of charge collection near the quarter-circle edge. A small loss in average charge in the final 50  $\mu\text{m}$  or so from the edge cannot be ruled out, but the drop is most likely just the precision on which the center of the circle is determined, which is about 50  $\mu\text{m}$ . No significant difference between the two guard-ring structure designs (middle and bottom pair of plots) is observed. Moreover, no significant differences between the unirradiated and irradiated detectors is seen.

## 5 Summary

Results from a test beam at the CERN SPS of 7 pre-prototype UT sensors, one p-in-n and 6 n-in-p, have been presented. The n-in-p sensors were irradiated at fluences of  $1.0 \times 10^{14} n_{\text{eq}}/\text{cm}^2$ ,  $1.8 \times 10^{14} n_{\text{eq}}/\text{cm}^2$  and  $4.0 \times 10^{14} n_{\text{eq}}/\text{cm}^2$ , and showed a gradual loss in total charge collected with increased dose. All detectors plateaued in the 300-400 V region, yielding a S/N of at least 15. This indicates that the anticipated 500 V maximum will be sufficient for operation of these detectors for the full  $50 \text{ fb}^{-1}$  data set expected to be collected in Run III of LHCb.

We also find that the irradiated n-in-p DUTs have substantially larger cluster sizes at normal incidence, compared to either the unirradiated n-in-p DUT, or the  $0.27 \times 10^{14} n_{\text{eq}}/\text{cm}^2$  p-in-n DUT. These larger clusters sizes at normal incidence are accompanied by improved position resolution, as one expects when there is charge sharing between strips.

The dependence of the charge collection on the interstrip position has also been studied. For the irradiated n-in-p DUTs, it is found that about 15% less charge is collected when a track goes through the middle of two strips, relative to the amount collected when it passes through the center of a given strip. This is consistent with findings from other experiments. The efficiency as function of interstrip position has also been studied, and in all cases it is found to exceed about 99%.

The position resolution in the various sensors has also been investigated. At normal incidence, the irradiated detectors show substantially better position resolution than the unirradiated detector. This stems from the larger fraction of 2-strip clusters in the irradiated detectors. This goes against the conventional thinking that in irradiated detectors, less charge is collected, resulting in a reduction of the fraction of multi-strip clusters. At large angles, all detectors studied show improved spatial resolution, and the best resolution achieved is about  $8 \mu\text{m}$  at an incidence angle in the  $15 - 20^\circ$  range. A resolution of about  $6.5 \mu\text{m}$  is found for the subset of 2-strip clusters.

The charge collection close to the circular portion of the DUTs was studied, and there no indication of any significant degradation of charge collection in the region close to this region. Moreover, there is no clear difference between the two different guard-ring structures along this boundary.

## Acknowledgements

We express our gratitude to our colleagues in the CERN accelerator departments for the excellent performance of the SPS. INFN (Italy); MNiSW and NCN (Poland); SNSF and SER (Switzerland); and NSF (USA). We also acknowledge the efforts of the VELO TimePix3 group for providing a high precision telescope to enable many of the studies presented in this paper.

## References

- [1] LHCb collaboration, *LHCb inner tracker: Technical Design Report*, CERN-LHCC-2002-029. LHCb-TDR-008.
- [2] LHCb collaboration, *LHCb reoptimized detector design and performance: Technical Design Report*, CERN-LHCC-2003-030. LHCb-TDR-009.
- [3] LHCb collaboration, *LHCb VELO Upgrade Technical Design Report*, CERN-LHCC-2013-021. LHCb-TDR-013.
- [4] LHCb collaboration, *LHCb Tracker Upgrade Technical Design Report*, CERN-LHCC-2014-001. LHCb-TDR-015.
- [5] LHCb collaboration, *LHCb Trigger and Online Technical Design Report*, CERN-LHCC-2014-016. LHCb-TDR-016.
- [6] Micron Semiconductor Ltd., <http://www.micronsemiconductor.co.uk>.
- [7] K. Akiba *et al.*, *The Timepix telescope for high performance particle tracking*, Nucl. Instrum. Meth. **A723** (2013) 47, [arXiv:1304.5175](https://arxiv.org/abs/1304.5175).
- [8] See Alibava systems web page at <http://www.alibavasystems.com>.
- [9] J. Bernabeu *et al.*, *A portable telescope based on the ALIBAVA system for test beam studies*, Nucl. Instrum. Meth. **A732** (2013) 130.
- [10] ALIBAVA Collaboration, R. Marco-Hernandez, *Development of a beam test telescope based on the ALIBAVA readout system*, JINST **6** (2011) C01002.
- [11] R. Marco-Hernandez, *A portable readout system for microstrip silicon sensors (ALIBAVA)*, IEEE Trans. Nucl. Sci. **56** (2009) 1642.
- [12] See Beetle manual  
[http://www.kip.uni-heidelberg.de/lhcb/Publications/BeetleRefMan.v1\\_3.pdf](http://www.kip.uni-heidelberg.de/lhcb/Publications/BeetleRefMan.v1_3.pdf).
- [13] S. Loechner, *Development, optimisation and characterisation of a radiation hard mixed-signal readout chip for LHCb*, PhD thesis, Heidelberg University, 2006, See Table 6.11 in CERN-THESIS-2006-061.
- [14] G. Kramberger *et al.*, *Charge collection properties of heavily irradiated epitaxial silicon detectors*, Nucl. Instrum. Meth. **A554** (2005) 212.
- [15] G. Casse, *P-type sensor results from the RD50 collaboration*, Proceedings of the 16<sup>th</sup> International Conference on Vertex Detectors (Vertex2007), Sept. 23-28. 2007, Lake Placid, NY USA. Published online in the Proceedings of Science PoS (VERTEX 2007) 021 .

- [16] G. Casse, *CCE studies in silicon*, Proceedings of the 17<sup>th</sup> International Conference on Vertex Detectors (Vertex2008), July 28-Aug. 1, 2008, Veluwe, the Netherlands. Published online in the Proceedings of Science PoS (VERTEX 2009) 036 .
- [17] M. Artuso, *Silicon sensors implemented on p-type substrates for high radiation resistance applications*, Nucl. Instrum. Meth. **A582** (2007) 835, [arXiv:physics/0701270](https://arxiv.org/abs/physics/0701270).
- [18] J. C. Wang, *LHCb VELO Upgrade*, Proceedings of the 18<sup>th</sup> International Conference on Vertex Detectors (Vertex2009), Sept. 13-18, 2009, Uto Island, Sweden. Published online in the Proceedings of Science PoS (VERTEX 2009) 037 .
- [19] A. Affolder, P. Allport, and G. Casse, *Collected charge of planar silicon detectors after pion and proton irradiations up to  $2.2 \times 10^{16} n_{eq} cm^{-2}$* , Nucl. Instrum. Meth. **A623** (2010) 177.
- [20] T. J. Brodbeck and A. Chilingarov, *Simulation of charge collection and sharing in microstrip detectors*, Nucl. Instrum. Meth. **A395** (1997) 29.
- [21] F. Campabadal *et al.*, *Beam tests of ATLAS SCT silicon strip detector modules*, Nucl. Instrum. Meth. **A538** (2005) 384.